Article

Not peer-reviewed version

Catalytic Performance of Metal Oxide-Based Catalysts in the Synthesis of Glycerol Carbonate: Toward Green Valorization of Glycerol

Mirna Lea Charif , Rami Doukeh * , Dragos Mihael Ciuparu *

Posted Date: 11 April 2025

doi: 10.20944/preprints202504.0772.v1

Keywords: mixed metal oxide catalysts; glycerol carbonate synthesis; acid-base catalysts

Preprints.org is a free multidisciplinary platform providing preprint service that is dedicated to making early versions of research outputs permanently available and citable. Preprints posted at Preprints.org appear in Web of Science, Crossref, Google Scholar, Scilit, Europe PMC.

Copyright: This open access article is published under a Creative Commons CC BY 4.0 license, which permit the free download, distribution, and reuse, provided that the author and preprint are cited in any reuse.

Preprints.org (www.preprints.org) | NOT PEER-REVIEWED | Posted: 11 April 2025

doi:10.20944/preprints202504.0772.v1

Disclaimer/Publisher's Note: The statements, opinions, and data contained in all publications are solely those of the individual author(s) and contributor(s) and not of MDPI and/or the editor(s). MDPI and/or the editor(s) disclaim responsibility for any injury to people or property resulting from any ideas, methods, instructions, or products referred to in the content.

Article

Catalytic Performance of Metal Oxide-Based Catalysts in the Synthesis of Glycerol Carbonate: Toward Green Valorization of Glycerol

Mirna Lea Charif [1], Rami Doukeh [2] and Dragoș Mihael Ciuparu [1],*

[1] Department of Petroleum Refining Engineering and Environmental Protection, Petroleum-Gas University of Ploiesti, 39 Bucharest Blvd., 100680 Ploiesti, Romania; mirnalea.charif@gmail.com (M.L.C.); dciuparu@upg-ploiesti.ro (D.M.C.).

[2] Department of Well Drilling, Extraction and Transport of Hydrocarbons, Petroleum-Gas University of Ploiesti, 39 Bucharest Blvd., 100680 Ploiesti, Romania; rami.doukeh@yahoo.com (R.D.).

* Correspondence: dciuparu@upg-ploiesti.ro (D.M.C.).

Abstract: The rising concern over carbon dioxide (CO_2) emissions has led to increased research on its conversion into value-added chemicals. Glycerol carbonate (GC), a versatile and eco-friendly compound, can be synthesized via the catalytic carbonylation of glycerol with CO_2. This study investigates the catalytic performance of three novel mixed metal oxide catalysts Ti-Al-Mg, Ti-Cr-Mg, and Ti-Fe-Mg, synthesized via co-precipitation. The catalysts were characterized using XRD, SEM, XPS, FTIR, TGA-DTG, and nitrogen adsorption–desorption isotherms. Among the tested systems, Ti-Al-Mg demonstrated the highest surface area, optimal porosity, and a balanced acid-base profile, resulting in superior catalytic activity. Under optimized conditions (175 °C, 10 bar CO_2, 4 h), Ti-Al-Mg achieved a maximum GC yield of 36.1%, outperforming Ti-Cr-Mg and Ti-Fe-Mg. The improved performance was attributed to the synergistic effects of its physicochemical properties, including high magnesium content and lower acidity, which favored CO_2 activation and glycerol conversion, while minimizing side reactions. These findings highlight the potential of tailored mixed metal oxide systems for efficient CO_2 immobilization and sustainable glycerol valorization.

Keywords: mixed metal oxide catalysts; glycerol carbonate synthesis; acid-base catalysts

1. Introduction

Carbon dioxide (CO_2) is recognized as one of the main greenhouse gases due to its significant and lasting impact on global climate change. In 2024, the atmospheric concentration of CO_2 reached approximately 422.5 parts per million (ppm), reflecting an increase of about 3 ppm compared to 2023 and a 50% rise over pre-industrial levels [1]. As a result, developing effective CO_2 mitigation strategies has become essential, including its capture and use as both an extraction solvent [2] and a feedstock for producing value-added chemicals, such as methanol, methane, mono-, di-, and tri-acetone, and 1,2-propanediol [3,4] Among these, glycerol carbonate (GC) stands out as a particularly valuable compound, not only for its industrial applications but also for its strategic role in valorizing bio-based glycerol [5].

To this end, glycerol carbonate is typically synthesized through the carbonylation of glycerol with CO_2 in the presence of heterogeneous catalytic systems, mainly based on metal oxides due to their ability to adsorb CO_2 on their surfaces. Heterogeneous catalysis offers significant advantages in this process, particularly in terms of catalyst separation and recyclability [6]. Gao et al. [5] reported the use of zeolite-based ETS-10 titanosilicate catalysts impregnated with active transition metals (Cu, Zn, Ni, Zr, Ce, Fe) for the efficient production of GC. Under reaction conditions of 170 °C, using Co/ETS-10 in the presence of CH_3CN as a dehydrating agent, a glycerol conversion of 35.0% and a GC yield of 12.7% were achieved.

© 2025 by the author(s). Distributed under a Creative Commons CC BY license.

Preprints.org (www.preprints.org) | NOT PEER-REVIEWED | Posted: 11 April 2025 doi:10.20944/preprints202504.0772.v1

Similarly, Yi-Hu Ke et al. [7] prepared CuO, NiO, Co_3O_4, ZrO_2, and Al_2O_3 via a hydrothermal method. Among these, CuO showed the best performance, achieving 89.0% glycerol conversion and 69.4% selectivity toward glycerol carbonate at 120 °C and 3.0 MPa CO_2 over 5 hours. In a separate study, Yi-Hu Ke et al. [8] used a CuO/Al_2O_3 catalyst prepared by impregnating activated alumina with an aqueous solution of $Cu(NO_3)_2{\cdot}3H_2O$. The 30% CuO/ Al_2O_3 catalyst, calcined at 700 °C, showed notable catalytic activity, reaching 41.3% glycerol conversion and a 17.5% GC yield at 150 °C and 4.0 MPa CO_2 over 5 hours. 2-Cyanopyridine was employed as both a dehydrating agent and a co-catalyst to enhance CO_2 activation.

In addition, glycerol carbonation with CO_2 was also investigated using various metal oxides (Fe, Zn, La, Ce, and Sn) prepared via the sol - gel method at 180 °C and 150 bar. ZnO showed the highest performance, yielding 8.1% glycerol carbonate after 12 hours of reaction [9].

Furthermore, the use of mixed metal oxide catalysts has been shown to increase the quantity and activity of moderate basic sites. Hongguang Li et al. [10] synthesized a series of La/Zn mixed oxide catalysts with varying molar ratios. The $La_2O_2CO_3$ catalyst containing ZnO at a La/Zn atomic ratio of 0.25, calcined at 500 °C, achieved 30.3% glycerol conversion and a 14.3% GC yield. The improved performance was attributed to ZnO's role in increasing the concentration of moderate basic sites, facilitating the activation of both glycerol and CO_2.

In a related study, Yajin Li et al. [11] have developed a series of $xLa_2O_2CO_3$-ZnO catalysts via hydrothermal synthesis to convert glycerol and CO_2 into glycerol carbonate through photothermal catalysis. The synergistic effect of light and heat, along with the interaction between ZnO and $La_2O_2CO_3$, enhanced catalytic performance. The 20% $La_2O_2CO_3$-ZnO catalyst achieved 6.9% glycerol conversion under reaction conditions of 150 °C, 5.5 MPa CO_2, and 6 hours.

Moreover, cerium–zirconium mixed oxide catalysts with varying Zr doping levels, $Ce_{(1-x)}Zr_xO_2$ ($x = 0 - 1$) [12] were studied to assess the effect of Zr incorporation on the catalytic activity. Increasing the Zr molar fraction from $x = 0$ to $x = 0.02$ significantly improved glycerol conversion (from 25.5% to 40.9%) and GC yield (from 21.4% to 36.3%). However, further zirconium addition reduced catalytic performance, with conversion and yield dropping to 25.9% and 21.7%, respectively, at $x = 0.2$.

Finally, Hongguang Li et al. [13] synthesized a series of Zn/La/Al/M catalysts (M = Li, Mg, Zr) derived from hydrotalcite-like compounds via co-precipitation. Incorporating Li, Mg, and Zr significantly enhanced catalytic activity. Under optimized conditions (7.0 mL CH_3CN, 0.14 g catalyst, 170 °C, 14 h, CO_2 pressure = 6.0 MPa), the Zn/La/Al/Li catalyst achieved a glycerol conversion of 39.5% and a glycerol carbonate yield of 18.7%.

In this study, three mixed metal oxide catalysts Ti-Al-Mg, Ti-Cr-Mg, and Ti-Fe-Mg were synthesized via co-precipitation, and evaluated for their performance in converting glycerol and CO_2 into glycerol carbonate in the attempt to tune the acid-base functions of the catalytic surface. Structural and surface characterizations (XRD, SEM, BET, XPS) revealed that, among the synthesized catalysts, Ti-Al-Mg had the highest surface area, well-developed porosity, and optimal acid-base site distribution. Among the catalysts tested, Ti-Al-Mg demonstrated superior catalytic performance reflected in the highest glycerol carbonate yield of 36.1% at 175 °C and 10 bar CO_2 over 4 hours, attributed to its homogeneous structure and well-balanced acid–base properties.

2. Catalyst Characterization

The catalysts were thoroughly characterized using various analytical techniques, including X-ray diffraction (XRD), scanning electron microscopy (SEM), thermogravimetric analysis (TGA-DTG), textural analysis (N_2 adsorption/desorption), X-ray photoelectron spectroscopy (XPS), and Fourier-transform infrared spectroscopy (FTIR).

XRD measurements were conducted at room temperature using a Bruker X-ray diffractometer (Karlsruhe, Germany; θ-θ type) equipped with a Cu-Kα radiation source ($\lambda = 1.5418$ Å), operating at 40 kV and 5 mA. The scans covered a 2θ range of 5–80° at a rate of 10°/min.

The microstructural morphology was examined using a scanning electron microscope (SEM) from FEI Company (Hillsboro, OR, USA).

Preprints.org (www.preprints.org) | NOT PEER-REVIEWED | Posted: 11 April 2025 doi:10.20944/preprints202504.0772.v1

Thermogravimetric and derivative thermogravimetric analyses (TGA-DTG) were performed on a METTLER TOLEDO TGA/IST Thermal Analysis System (Greifensee, Switzerland) within the temperature range of 25–600 °C, under a nitrogen atmosphere, with a heating rate of 10 °C/min. The textural properties of the prepared catalysts were evaluated using a Quantachrome NOVA 2200e Gas Sorption Analyzer.

The nitrogen adsorption/desorption isotherms were recorded at 77.35 K across a relative pressure (p/p0) range of 0.005 to 1.0. Data processing was carried out using the NovaWin version 11.03 software. The specific surface area was calculated using the BET (Brunauer–Emmett–Teller) method, while the total pore volume was estimated from the desorbed volume at a relative pressure near unity, utilizing the BJH (Barrett–Joyner–Halenda) method. Measurement of the adsorption/desorption isotherms were performed using a Quantachrome Nova 2200e instrument (Boynton Beach, FL, USA).

The surface chemistry was studied by X-ray Photoelectron Spectroscopy (XPS) using a K-Alpha instrument from Thermo Scientific (Thermo Fisher Scientific, Waltham, MA, USA), with a monochromatic Al Kα source (1486.6 eV), at a bass pressure of 2×10^{-9} mbar. Charging effects were compensated by a flood gun and binding energies were calibrated by placing the C1s peak at 284.4 eV as internal standard. A pass energy of 200 eV and 20 eV was used for survey and high-resolution spectra acquisition, respectively.

3. Experimental

3.1. Materials and Methods

3.1.1. Materials

Titanium (IV) butoxide (Merck, 97%), $Al(NO_3)_3·9H_2O$ (Merck, 99%), $Mg(NO_3)_2·6H_2O$ (Merck - Sigma-Aldrich, BioUltra, ≥99.0%), $Cr(NO_3)_3·9H_2O$, (Merck, 99%), $FeCl_3·6H_2O$ (Carl Roth, Karlsruhe, Germany, min. 98%), Carbon dioxide CO_2 (SIAD Romanian, Purity: ≥ 99.5%, Glycerol (Gly) (Merck, ≥99.5%), Acetonitrile (Amex-lab, ≥99.9%) and Glycerol carbonate (GC) (Merck -Sigma-Aldrich, ≥99%).

3.1.2. Catalysts Preparation

The nanostructured Ti-(Me)-Mg catalysts; where Me represents metal ions such as Cr^{3+}, Al^{3+}, and Fe^{3+}; were synthesized via a co-precipitation method. This approach involved the reaction of titanium (IV) butoxide with nitrate salts of Al^{3+} and Mg^{2+}, and with a chloride salt of Fe^{3+}, maintaining a fixed molar ratio of Ti:Me:Mg = 2:1:1. To prepare Ti-Al-Mg, 27.23 g of titanium (IV) butoxide, 15.00 g of $Al(NO_3)_3·9H_2O$, and 10.62 g of $Mg(NO_3)_2·6H_2O$ were used. In the case of Ti-Fe-Mg, 27.23 g of titanium (IV) butoxide, 10.80 g of $FeCl_3·6H_2O$, and 10.62 g of $Mg(NO_3)_2·6H_2O$ were used. For Ti-Cr-Mg, the synthesis involved 27.23 g of titanium (IV) butoxide, 11.65 g of $Cr(NO_3)_3·9H_2O$, and 10.62 g of $Mg(NO_3)_2·6H_2O$.

For each catalyst, the precursors were dissolved in 500 mL of absolute ethanol. To ensure complete dissolution, the pH was adjusted to 3.0 using concentrated nitric acid. The solution was stirred at 60°C, and ammonia solution (25 wt%) was added dropwise until the pH reached 10-11, leading to the precipitation of nanoparticles. The mixture was stirred for an additional 45 minutes. After the reaction, the nanoparticles were separated by centrifugation and washed with distilled water. The nanoparticles were then washed with ethanol, dried for 2 hours at 150°C, and calcined at 450 °C for 4 hours with a heating rate of 10 °C/min. The calcination temperature was selected based on the thermal stability of the nanoparticles before calcination.

3.1.3. Experimental Setup and Procedure for Catalysts' Testing in Glycerol Carbonate Synthesis

The experimental program for the synthesis of glycerol carbonate was carried out using a batch-type BERGHOF installation. The main component is a stainless-steel autoclave-type reactor with a

Preprints.org (www.preprints.org) | NOT PEER-REVIEWED | Posted: 11 April 2025 doi:10.20944/preprints202504.0772.v1

working volume of 600 mL, equipped with a turbine-type mechanical stirrer (up to 2000 rpm), sealed at the reactor lid using a packing gland system. The setup includes sensors for temperature, pressure, and rotational speed. Heating is provided by an electric mantle with a temperature control system. The reactor lid is equipped with the following ports: a gas inlet for volatile reactants or inert gases, a controlled gas outlet connected to a purge system for depressurization, and a safety valve, also linked to the purge line.

Using this setup, the experimental procedure was carried out as follows: a mixture of 25 g of glycerol and 50 mL of acetonitrile serving as dehydrating agent to shift the unfavorable equilibrium towards the product side and enhance the selectivity for glycerol carbonate [14,15], was introduced into the reaction vessel. Dried catalyst was subsequently added at room temperature and the reactor was immediately closed and purged for 5 minutes with nitrogen gas. Subsequently the reaction temperature was gradually increased, while maintaining continuous mechanical stirring of the glycerol-catalyst-acetonitrile mixture. Once the desired temperature was reached, carbon dioxide gas was introduced into the system until the desired pressure was reached, initiating the reaction, which proceeded for 4 hours.

Upon completion of the reaction time, the autoclave was allowed to cool naturally to room temperature, followed by the controlled release of pressure. The liquid phase was then separated from the catalyst through centrifugation. The recovered catalyst was washed with ethanol and deionized water, followed by drying at 80 °C overnight to ensure complete removal of residual solvents. The liquid phase was subjected to analysis using gas chromatography with a flame ionization detector (GC-FID, Varian 3800). The gas chromatograph is equipped with a ZB-5ms column (L=30 m, D=250 µm, d=0.25 µm) and Helium (He) was used as the carrier gas at a flow rate of 1 mL/min.

The oven thermal program was initiated at 100 °C with a heating rate of 5 °C/min until reaching 250 °C, where it was maintained for 1 minute. The injector temperature was set to 250°C, and the injected sample volume was 1 µL.

To quantify the concentration of glycerol carbonate in the final product, a calibration curve was established, as shown in Figure 1, using acetonitrile as the solvent. The calibration curve was constructed over a glycerol carbonate concentration range of 1 to 90% by weight.

The yield was calculated based on the following equation:

$$\%Yield\ of\ GC = \frac{moles\ of\ \mathrm{GC}}{moles\ of\ \mathrm{Gly\ introduced}}.$$

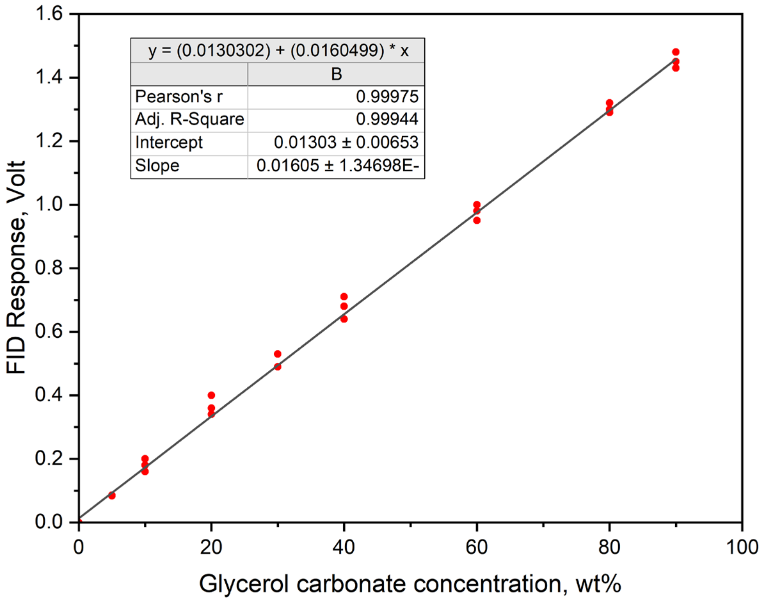

Figure 1. Calibration curve used for calculation of glycerol carbonate concentration.

Preprints.org (www.preprints.org) | NOT PEER-REVIEWED | Posted: 11 April 2025 doi:10.20944/preprints202504.0772.v1

4. Results and Discussions

4.1. Catalyst Characterization

The crystalline phases of the active components in the nano-catalysts Ti-Al-Mg, Ti-Cr-Mg, and Ti-Fe-Mg were identified using X-ray diffraction (XRD), as depicted in Figure 2. The resulting diffraction patterns were analyzed with the aid of the "Match!" software, and phase identification was validated through cross-referencing with reliable crystallographic databases and peer-reviewed literature.

All catalysts exhibited characteristic diffraction peaks at 2θ = 25.37°, 38.25°, 48.80°, 54.65°, and 62.75°, corresponding to the crystalline phases of $MgTi_2O_5$ [16,17], TiO_2 [18,19], Ti_3O_5 [18,20,21], TiO_2 [18,19], and MgO [22,23], respectively.

In the case of Ti-Al-Mg, a distinct peak was observed at 2θ ≈ 47.45°, which was attributed to the formation of the ternary oxide phase $MgAl_2Ti_3O_{10}$ [24]. Notably, no reflections corresponding to binary aluminum-magnesium oxides, such as $MgAl_2O_4$, or to aluminum oxide (Al_2O_3) were detected, indicating that the ternary phase is the dominant crystalline form in this system.

Conversely, the Ti-Fe-Mg and Ti-Cr-Mg catalysts exhibited additional diffraction peaks at 2θ = 64.10° and 36.17° which were assigned to the spinel-type binary oxides $MgFe_2O_4$ [23,25,26] and Cr_2MgO_4 [23], respectively. No evidence of ternary oxide phase formation was observed in either system.

Furthermore, the XRD diffractograms revealed the presence of monometallic oxide phases. In Ti-Fe-Mg, a peak at 2θ = 33.27° was consistent with the hematite phase of Fe_2O_3 [27], while the Ti-Cr-Mg catalyst exhibited a peak at 2θ = 41.23°, corresponding to the crystalline phase of Cr_2O_3 [28].

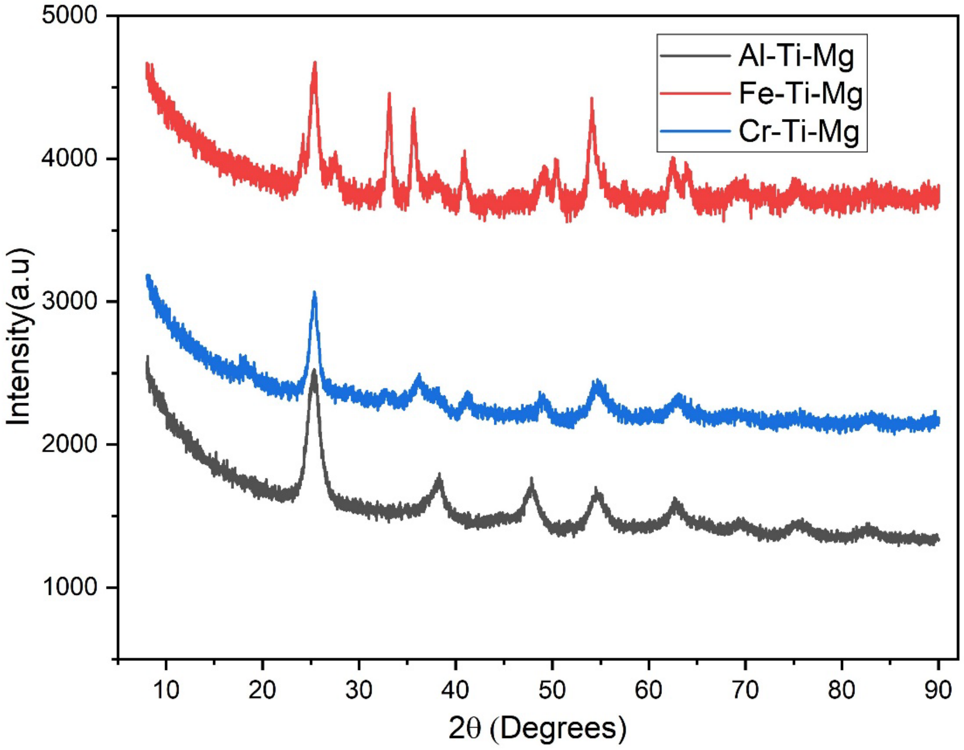

Figure 2. XRD patterns of Ti-Al-Mg, Ti-Cr-Mg and Ti-Fe-Mg.

The crystallite size (D) of the catalysts were calculated using the Debye-Scherrer equation (1) [29]:

$$D=\frac{k\cdot\lambda}{\beta\cdot\cos\theta} \qquad (1)$$

In the equation employed for crystal size estimation, λ represents the wavelength of the X-ray radiation used (Cu Kα = 0.15406 nm), β denotes the full width at half maximum (FWHM) of the diffraction peak, and θ corresponds to the Bragg diffraction angle. The constant k, known as the shape factor, is typically assumed to have a value of 0.98. Based on this equation, the average crystallite sizes of the phases formed during the preparation of the Ti-Al-Mg, Ti-Cr-Mg, and Ti-Fe-Mg catalysts were calculated, as presented in Table 1.

Table 1. Oxide Types and Calculated Crystallite Sizes of the Phases in Ti-Al-Mg, Ti-Fe-Mg, and Ti-Cr-Mg Catalysts Based on X-Ray Diffraction (XRD) Patterns.

2θ	**Ti-Al-Mg**		**Ti-Fe-Mg**		**Ti-Cr-Mg**	
	Oxide type	**Crystallite size (nm)**	**Oxide type**	**Crystallite size (nm)**	**Oxide type**	**Crystallite size (nm)**
25.37	$MgTi_2O_4$	0.087	$MgTi_2O_4$	0.143	$MgTi_2O_4$	0.116
33.27	-	-	Fe_2O_3	0.249	-	-
36.17	-	-	-	-	Cr_2MgO_4	0.092
38.25	TiO_2	0.062	TiO_2	0.276	TiO_2	0.074
41.23	-	-	-	-	Cr_2O_3	0.135
47.45	$MgAl_2Ti_3O_{10}$	0.108	-	-	-	-
48.80	-	-	Ti_3O_5	0.268	Ti_3O_5	0.149
54.65	TiO_2	0.088	TiO_2	0.224	TiO_2	0.086
62.75	MgO	0.090	MgO	0.172	MgO	0.106
64.10	-	-	$MgFe_2O_4$	0.237	-	-

The XPS spectra of the prepared catalysts, as shown in Figure 3, confirm the presence of Mg, Ti, and O in all samples, as evidenced by the characteristic peaks of Mg 1s, Mg 2p, Ti $2p_{3/2}$, Ti $2p_{1/2}$, and O 1s. The Mg 1s peak at approximately 1303.20 eV indicates the successful incorporation of magnesium through Mg-O bonding, while the Mg 2p signal around 50.1 eV suggests the presence of Mg-OH groups [30]. High-resolution Ti 2p spectra reveal a well-defined Ti $2p_{3/2}$ peak at ~458 eV and a weaker Ti $2p_{1/2}$ peak at ~464 eV, consistent with Ti^{4+} species forming Ti-O bonds [16]. The O 1s peak at 530.70 eV corresponds to lattice oxygen associated with Mg^{2+}, Al^{3+}, and Ti^{4+}, further confirming the formation of Ti-O, Al-O, and Mg-O bonds [24,31].

These observations are in agreement with XRD analysis, which shows the formation of crystalline phases such as TiO_2, MgO, and the binary oxide $MgTi_2O_5$ with an orthorhombic crystal structure [32]. The Ti 2p binding energies confirm the presence of Ti^{4+}, as expected in TiO_2 and $MgTi_2O_5$, while the Mg 1s signal indicates Mg^{2+} in accordance with the known crystal structures.

In the case of the Ti-Al-Mg catalyst, the Al 2p and Al 2s peaks at 73.9 and 117.8 eV, respectively, indicate oxidized aluminum forming Al-O bonds [24]. These findings are supported by XRD results that confirm the formation of the ternary oxide phase $MgAl_2Ti_3O_{10}$, which arises due to cation substitution phenomena, specifically the replacement of Al^{3+} by Ti^{4+} within the oxide lattice, leading to a homogenous crystalline network [24,33]. Such substitutions induce changes in the crystal structure and are consistent with literature reports describing Ti-Al-Mg as a well-structured mixed-metal oxide catalyst with strong metal-oxygen interactions, which contribute to its enhanced performance in glycerol carbonate synthesis.

In contrast, no ternary oxide formation was observed for Ti-Cr-Mg and Ti-Fe-Mg catalysts. The XPS spectrum of Ti-Cr-Mg confirms the presence of chromium through the Cr 2p peak at ~579 eV, indicating the formation of Cr-O bonds within a mixed-metal oxide matrix. The O 1s peak is associated with lattice oxygen bonded to Mg^{2+}, Cr^{3+}, and Ti^{4+}, supporting the presence of Ti-O, Cr-O, and Mg-O bonds. These results are in line with XRD findings showing the formation of Cr_2MgO_4 with a classical AB_2O_4 spinel structure and Cr_2O_3 [34,35], reinforcing the presence of a well-defined oxide network with strong metal-oxygen interactions [31,36].

Similarly, the XPS spectrum of the Ti-Fe-Mg catalyst reveals Mg, Ti, O, and Fe species. The Fe 2p signal at approximately 712.20 eV corresponds to Fe^{3+} species forming Fe-O bonds (Fe_2O_3) [14,31]. XRD analysis confirms the formation of $MgFe_2O_4$, a binary oxide with a classical spinel structure of the AB_2O_4 type [34,37,38].

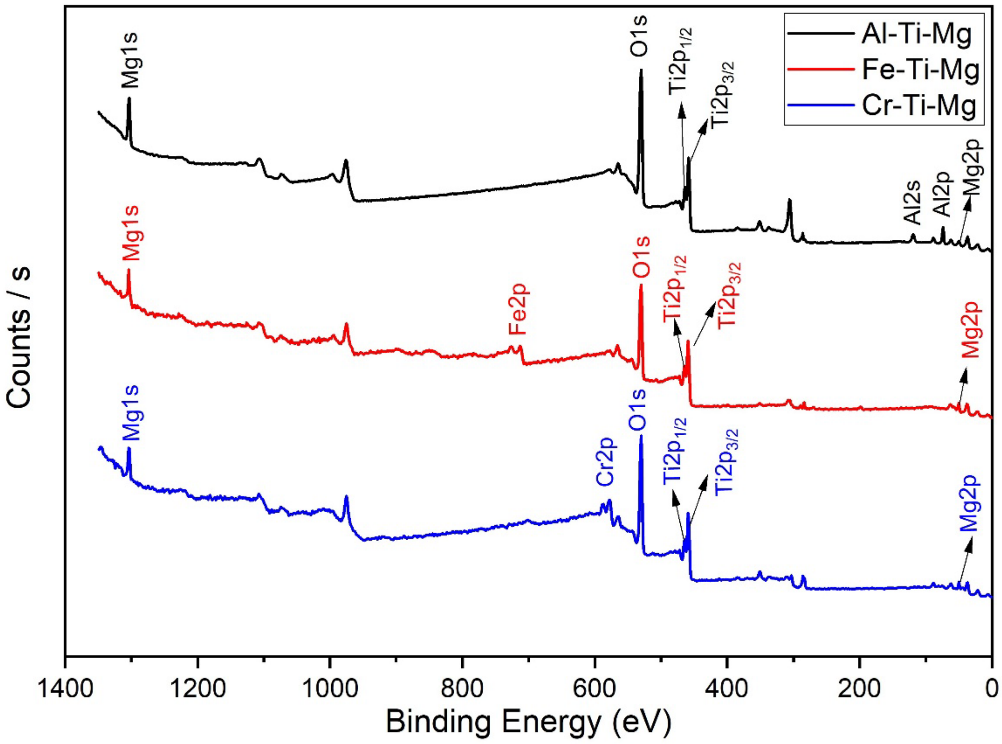

Figure 3. XPS Analysis of Ti-Al-Mg, Ti-Cr-Mg, and Ti-Fe-Mg.

Figure 4 presents SEM images of the porous catalysts, revealing distinct morphological features across the prepared catalysts. The Ti-Al-Mg catalyst shows a porous, rough surface, and agglomerated surface, composed of irregularly shaped particles with layered and compact structures. This morphology suggests the presence of an extended network of pores and interparticle voids, which facilitates effective molecular diffusion. The roughness and porosity provide a large number of exposed active sites, allowing for efficient adsorption and activation of reactants. These features indicate minimal diffusion resistance and are generally associated with high catalytic activity due to the enhanced accessibility of internal active regions [39,40].

In contrast, the Ti-Cr-Mg catalyst exhibits a more agglomerated morphology with fewer visible pores and irregular particle shapes. The agglomeration reduces the external surface area and blocks the internal porosity, creating diffusion constraints. Such morphology limits the penetration of glycerol and CO_2 into the catalyst structure, reducing the contact between reactants and catalytic sites. This structural feature is consistent with the findings of Granados-Reyes et al. [41], who observed that Cr-containing Mg-based catalysts exhibited decreased catalytic performance due to agglomeration-induced diffusion resistance and reduced site availability.

The Ti-Fe-Mg catalyst further emphasizes this limitation. SEM images show a fragmented, dense and heterogeneous surface with large agglomerates and significantly restricted porosity. The compact arrangement of particles and lack of interconnected pores severely hinder internal diffusion, especially under liquid-phase reaction conditions where glycerol's high viscosity further reduces mass transport. These morphological features impose substantial diffusion limitations, restricting the effective utilization of catalytic sites. Singh et al. [42] reported similar observations in Fe-based catalysts for glycerol carboxylation, where particle agglomeration and low porosity resulted in low CO_2 activation and reduced catalytic activity.

In summary, the SEM images of Ti-Cr-Mg and Ti-Fe-Mg catalysts reveal morphologies that significantly restrict reactant diffusion. The agglomerated, dense structures with limited porosity create diffusion barriers, leading to poor catalyst performance due to reduced accessibility of active sites.

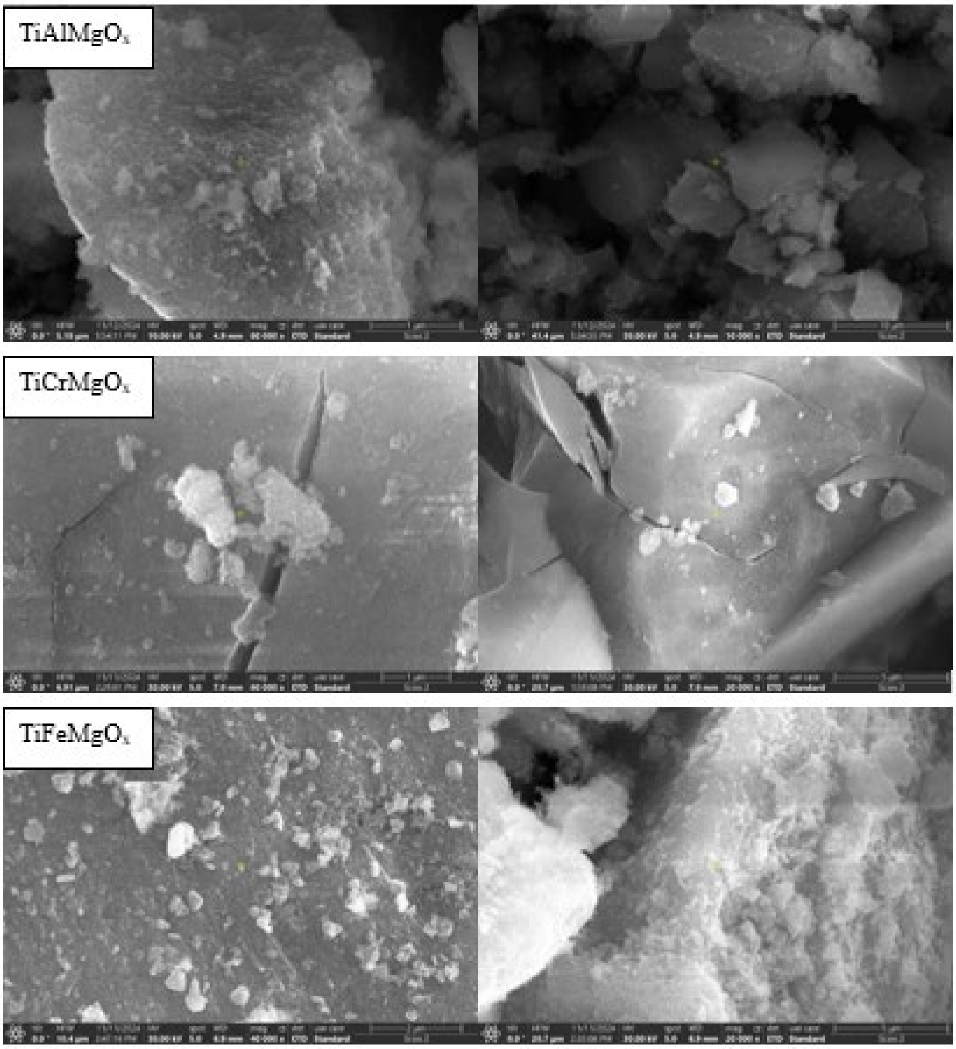

Figure 4. SEM images of Ti-Al-Mg, Ti-Cr-Mg, and Ti-Fe-Mg.

The EDS analysis in Figure 5 confirms the successful formation of a Ti-Al-Mg oxide structure in the Ti-Al-Mg catalyst, as evidenced by the presence of Ti, Al, Mg, O, C, and N, with significant contributions from oxygen (64.09%), aluminum (23.51%), and magnesium (6.61%). Elemental mapping further reveals a uniform distribution of these key elements, which supports improved catalytic efficiency and thermal stability [24].

In comparison, the EDX spectrum of Ti-Cr-Mg shows the presence of Ti, Cr, Mg, and O, with chromium contributing 21.99%. While Cr incorporation enhances moderate Lewis's acidity and structural stability, the elemental mapping displays a slightly less homogeneous distribution than in Ti-Al-Mg. This lower uniformity may hinder synergetic effects of acid-base sites ensured by different metal ions in proximity, behaving more like mechanical mixtures of different oxide phases. These results are in line with the findings of Granados-Reyes et al., who reported that Cr-based mixed oxides, though moderately effective, were limited by uneven elemental dispersion and lower acid site availability [41].

The EDX analysis of the Ti-Fe-Mg catalyst confirms the presence of Ti, Fe, Mg, and O, with Fe comprising 28.97%. Although Fe contributes weak acid sites, its high content may lead to the formation of less active species, likely due to a reduced pore volume. As shown in Table 2, the pore volume decreases to 0.166 cm^3/g compared to 0.345 cm^3/g for AL-Ti-Mg, which may hinder diffusion and catalytic activity. Additionally, elemental mapping reveals a non-uniform distribution of Fe, further reducing the number of effective catalytic sites. These findings are consistent with those

Preprints.org (www.preprints.org) | NOT PEER-REVIEWED | Posted: 11 April 2025 doi:10.20944/preprints202504.0772.v1

reported by Singh et al., where Fe-containing catalysts exhibited low performance due to uneven elemental dispersion and weak acidity [42].

The uneven elemental dispersion in the Cr- and Fe-containing catalysts resulted in the formation of single metal oxide clusters, leading to a reduction in surface area to 54.47 m²/g and 28.20 m²/g, respectively, as shown in Table 2. This decline in surface area consequently reduced the number of available active sites compared to the Al-Ti-Mg catalyst, which exhibits a surface area of 119.43 m²/g.

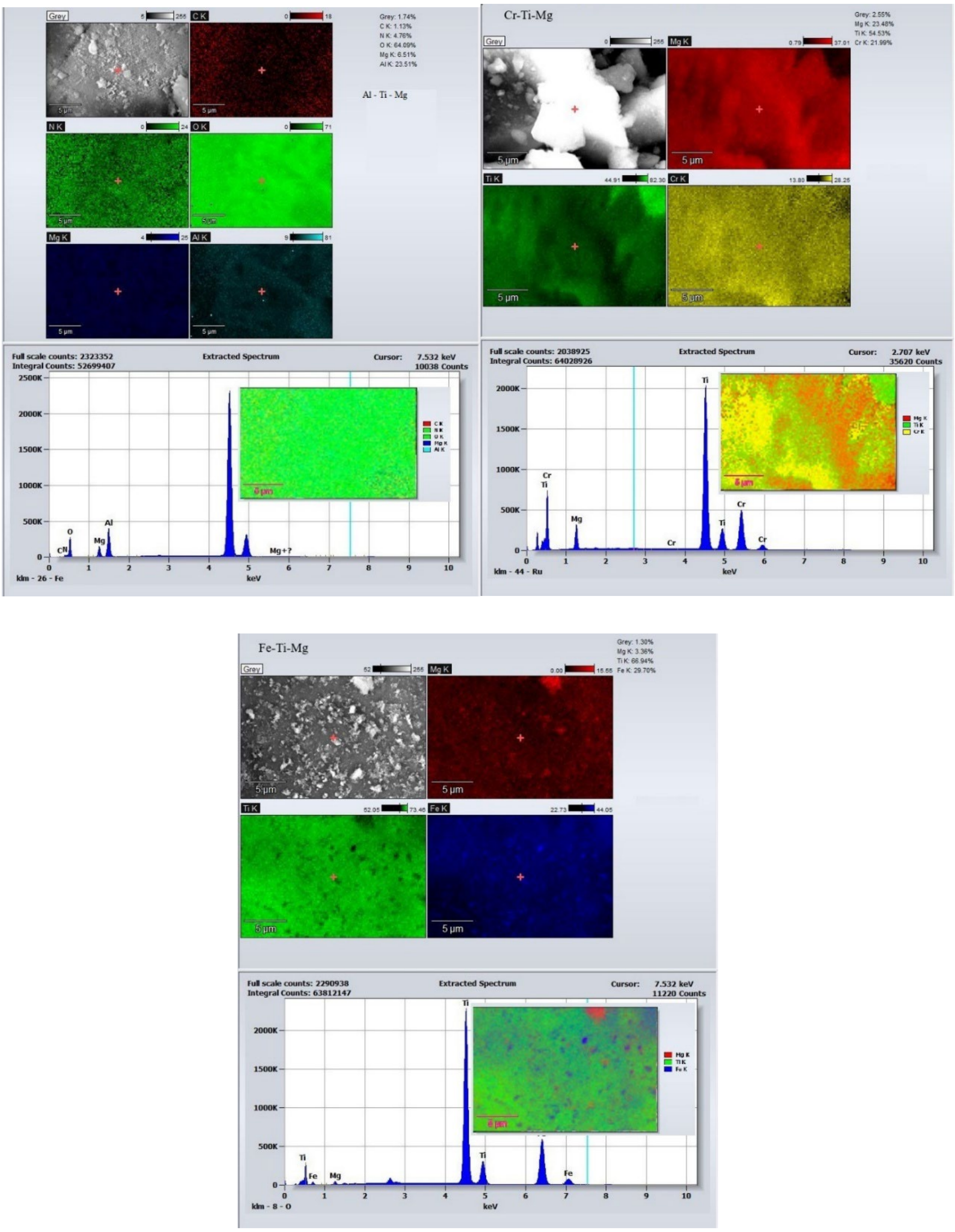

Figure 5. EDX spectra of Ti-Al-Mg, Ti-Cr-Mg, and Ti-Fe-Mg.

The nitrogen adsorption–desorption isotherms of the Ti-Al-Mg, Ti-Cr-Mg, and Ti-Fe-Mg catalysts (Figure 6) all exhibit type IV isotherms with H_2 hysteresis loops, characteristic of mesoporous structures with ink-bottle-shaped pores, according to IUPAC classification [43,44]. In all cases, the gradual increase in adsorption at low relative pressure ($P/P_0 < 0.3$) confirms the presence of micropores, while the sharp rise at higher pressures ($P/P_0 > 0.7$) indicates the existence of larger mesopores and some macropores.

However, differences in pore size distributions are observed. For Ti-Al-Mg and Ti-Cr-Mg, the inset graphs show sharp peaks around 3-5 nm, reflecting a dominant mesoporous region with limited expansion beyond 10 nm. This indicates a rather uniform porous textures, in line with literature reports [24,45], and confirms a well-structured pore network that supports catalytic performance [31].

In contrast, Ti-Fe-Mg exhibits a broader mesoporous distribution with a sharp peak between 8-12 nm and minimal extension beyond 20 nm. Despite the larger average pore size, the distribution remains relatively narrow, indicating a fairly uniform structure. These observations are consistent with reported findings in the literature [24,45], further supporting the classification and textural analysis of these catalysts.

Table 2 summarizes the surface area, pore volume, and pore width of the as-prepared catalysts. Among metal oxides, Ti-Al-Mg has the highest BET surface area (119.43 m^2/g) and pore volume (0.345 cm^3/g), confirming a highly mesoporous structure (6.81 nm pore width) that supports good adsorption and catalytic activity. Ti-Cr-Mg, with a moderate surface area (54.47 m^2/g) and slightly larger pores (7.12 nm), offers a balance between porosity and stability, making it suitable for catalysis, but less efficient than Ti-Al-Mg. Ti-Fe-Mg has the largest pores (10.68 nm), allowing better mass transfer, but its lower surface area (28.20 m^2/g) and moderate pore volume (0.166 cm^3/g) indicate a trade-off between adsorption capacity and catalytic efficiency, which aligns with literature studies [24,45].

Table 2. Textural properties of prepared catalysts.

Catalysts	BET surface area (m^2/g)	Pore volume (cm^3/g)	Average pore width (nm)
Ti-Al-Mg	119.43	0.345	6.81
Ti-Cr-Mg	54.47	0.193	7.12
Ti-Fe-Mg	28.20	0.166	10.68

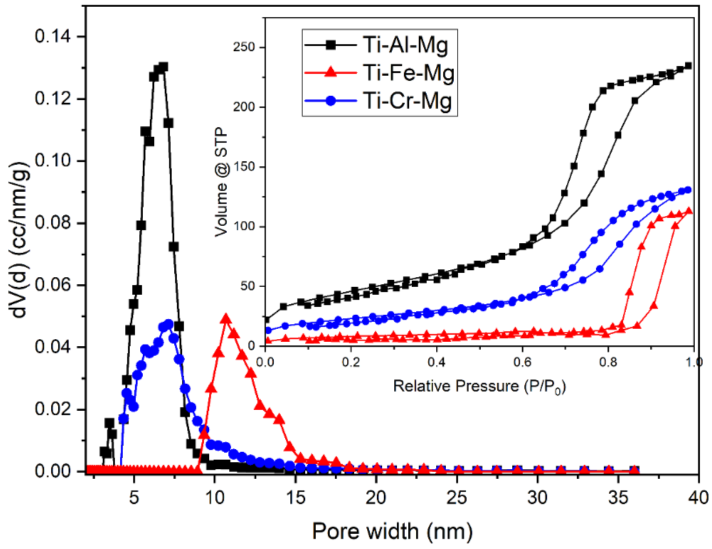

Figure 6. Nitrogen adsorption–desorption isotherms of Ti-Al-Mg, Ti-Cr-Mg, and Ti-Fe-Mg.

The thermal properties of the Ti-Al-Mg, Ti-Cr-Mg, and Ti-Fe-Mg catalysts were evaluated using thermogravimetric analysis (TGA) under nitrogen (N_2) flow. As shown in the TGA curves (Figure 7), all three samples exhibit an initial weight loss below 300 °C, which is attributed to the decomposition of adsorbed water and interlayer crystal water. These materials display minimal weight loss during heating, indicating high thermal stability across the series.

Preprints.org (www.preprints.org) | NOT PEER-REVIEWED | Posted: 11 April 2025 doi:10.20944/preprints202504.0772.v1

Between 300 °C and 600 °C, a gradual weight reduction is observed in all samples, corresponding to the decomposition of interlayered crystal water and hydroxyl (-OH) layers [4]. This steady mass loss reflects a stable thermal profile with no abrupt structural breakdown. The corresponding DTG curves for each catalyst further confirm this behavior, showing broad, low-intensity peaks that suggest a slow and continuous dehydration process rather than a sudden decomposition event [46].

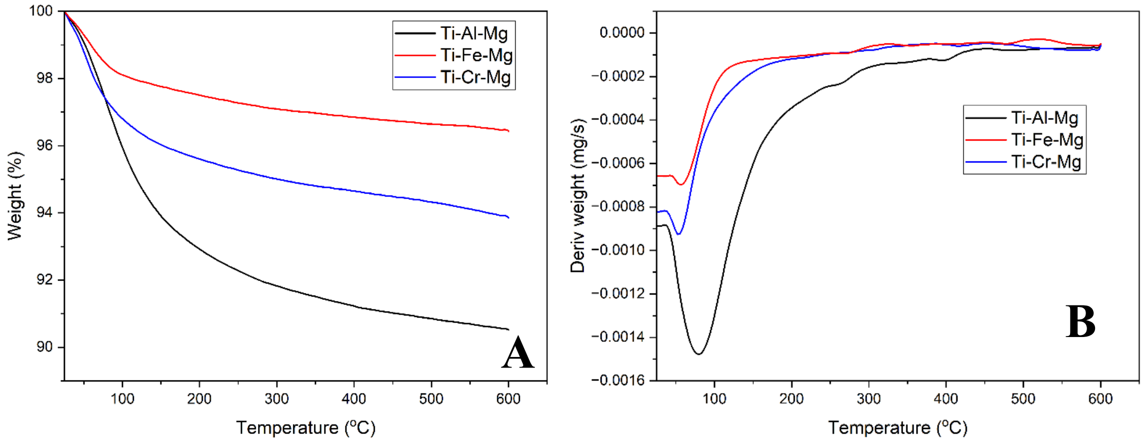

Figure 7. TGA (Fig 7A) -DTG (Fig 7B) patterns of Ti-Al-Mg, Ti-Cr-Mg, and Ti-Fe-Mg.

4.2. Catalysts Effect on Glycerol Carbonate Synthesis

Figure 8 shows the effect of temperature on glycerol carbonate yield using Al-Ti-Mg, Fe-Ti-Mg, and Cr-Ti-Mg catalysts at 5% catalyst-to-glycerol loading, 10 bar pressure, and a 4-hour reaction time.

For Al-Ti-Mg and Fe-Ti-Mg catalysts, the yield increased as the temperature rose from 130 °C to 175 °C. Beyond 175 °C, the yield with Al-Ti-Mg remained stable, while that with Fe-Ti-Mg began to decline. Specifically, Al-Ti-Mg produced a yield of 11.3% at 130 °C, which increased to 36.10% at 175 °C. In comparison, Fe-Ti-Mg showed a yield increase from 8.55% to 25.19% over the same temperature range, followed by a decrease to 17.35% at 200 °C. This decrease is attributed to the formation of undesired by-products resulting from side reactions, including glycerol dehydration and polymerization [47–49].

Cr-Ti-Mg, however, exhibited a significantly lower yield at 175 °C and 10 bar CO_2 pressure, over four times lower than Al-Ti-Mg and less than half that of Fe-Ti-Mg.

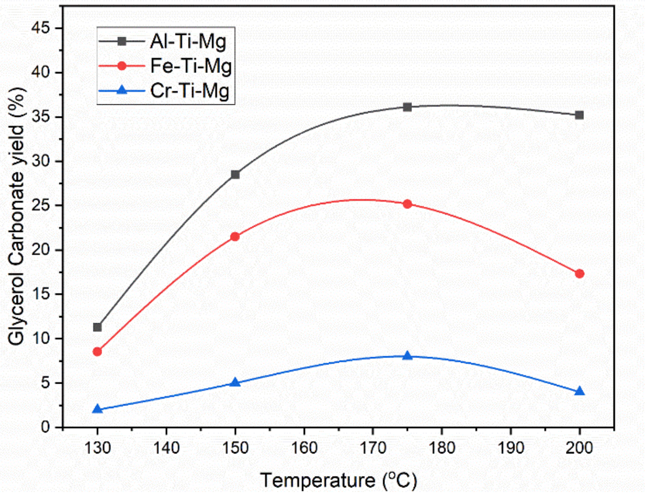

Figure 8. Effect of Temperature on Glycerol Carbonate yield.

Preprints.org (www.preprints.org) | NOT PEER-REVIEWED | Posted: 11 April 2025 doi:10.20944/preprints202504.0772.v1

The Al-Ti-Mg catalyst exhibits high efficiency due to its large specific surface area (119.43 m^2/g), which is more than four times greater than that of Fe-Ti-Mg (28.20 m^2/g), enhancing its capacity to adsorb reactants, as shown in Figure 6.

XRD and XPS analysis reveal the presence of iron oxides (Fe_2O_3) in Fe-Ti-Mg, which increase its acidity [50] and reduce its effectiveness in converting CO_2 and glycerol to glycerol carbonate. Additionally, SEM-EDX analysis shows that the magnesium content in Al-Ti-Mg is 6.51%, nearly double that of Fe-Ti-Mg (3.36%).

Although Cr-Ti-Mg has a moderate surface area (54.47 m^2/g) and high magnesium content, its catalytic performance is poor due to the strong acidity of chromium oxide, which is higher than that of iron and aluminum oxides. These findings align with previously reported literature, further validating the acidity-based classification of these metal oxide catalysts [51–53], thus hindering its activity in this reaction.

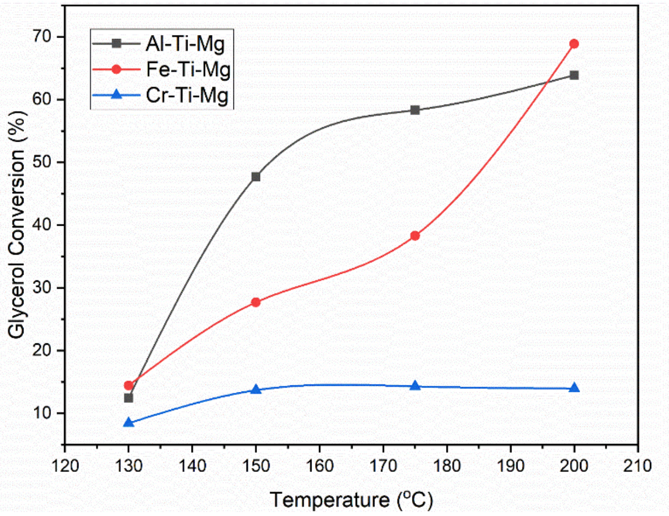

Figure 9. Effect of Temperature on Glycerol Conversion.

As shown in Figure 9, increasing the temperature enhances glycerol conversion. However, the glycerol carbonate yield remains relatively stable above 175 °C for Al-Ti-Mg, while it decreases for Fe-Ti-Mg beyond this point. This decline is attributed to the formation of undesired by-products from side reactions such as glycerol polymerization and thermal degradation [47–49].

The sharp drop in glycerol carbonate yield with Fe-Ti-Mg at temperatures above 200 °C is likely due to iron-catalyzed degradation of glycerol carbonate, which reduces reaction efficiency and leads to product loss to byproducts.

Figure 10 shows that increasing the catalyst concentration up to 10% improves glycerol carbonate yield for all catalysts. Al-Ti-Mg delivered the highest yield, followed by Fe-Ti-Mg and then Cr-Ti-Mg. A significant improvement was observed increasing the catalyst loading between 2.5% and 5%, while the increase at 10% gave only a marginal increase in glycerol carbonate yield, suggesting the reaction may be approaching a catalytic efficiency limit at higher concentrations.

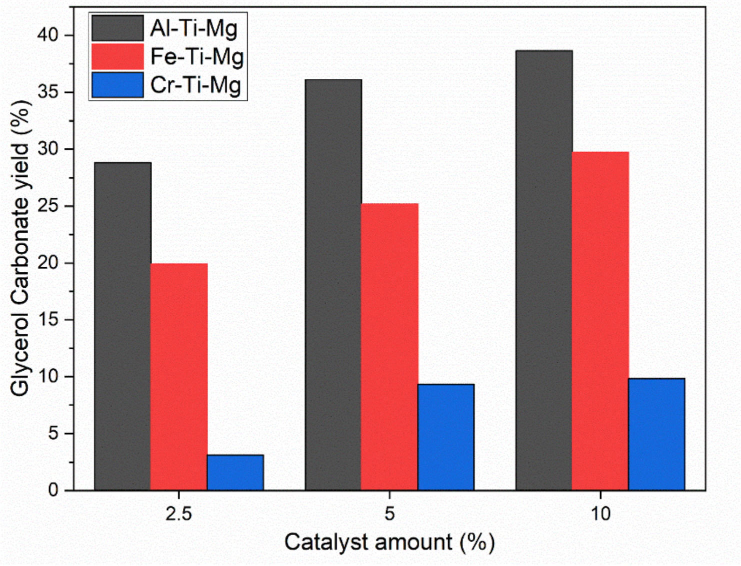

Figure 10. Effect of Catalyst Concentration on Glycerol Carbonate yield (%).

Similarly, as shown in Figure 11, glycerol conversion increased steadily with higher catalyst loading. Al-Ti-Mg again showed the highest conversion, followed by Fe-Ti-Mg and Cr-Ti-Mg. At 10% concentration, the conversion was significantly higher than at 2.5%, due to the increased number of active sites available at higher catalyst concentrations, which enhances both glycerol conversion and glycerol carbonate formation.

The superior performance of Al-Ti-Mg is attributed to its balanced acid–base properties, which play a key role in CO_2 activation and glycerol adsorption.

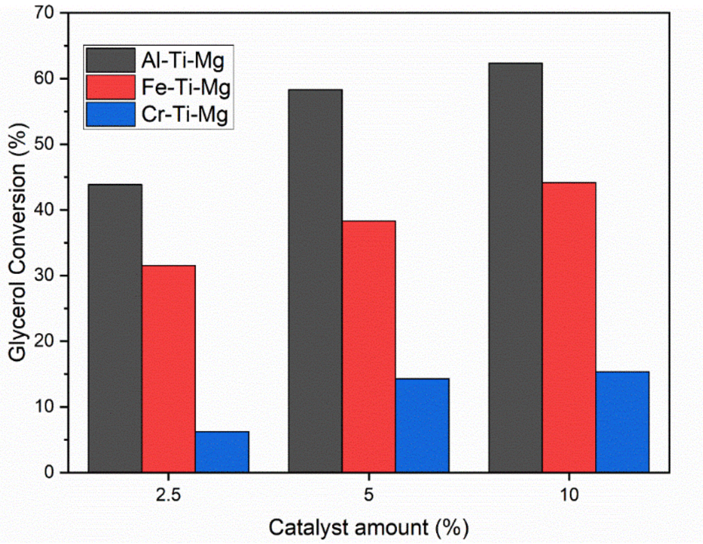

Figure 11. Effect of Catalyst concentration on Glycerol Conversion (%).

The catalytic performance follows the order: Al-Ti-Mg > Fe-Ti-Mg > Cr-Ti-Mg. This is attributed to Al-Ti-Mg's higher surface area, better porosity, and uniform magnesium content at the surface, which improves base sites at the surface. Its lower acidity also minimizes over-adsorption and suppresses undesired side reactions.

At 10% concentration, performance tends to stabilize, likely eliminating mass transfer limitations that might occur at lower catalyst loading concentration resulting to limited active sites available for reaction. Therefore, increasing catalyst concentration from 2.5% to 10% at 175 °C and 10 bar CO_2

pressure significantly improves both glycerol carbonate yield and glycerol conversion. However, the benefit beyond 5% is less pronounced, emphasizing the need to optimize catalyst loading for maximum efficiency without excess material use.

The catalytic performance of the synthesized mixed metal oxide catalysts (Ti-Al-Mg, Ti-Fe-Mg, and Ti-Cr-Mg) is governed by a complex interplay of surface composition, homogeneity, acid-base character, and textural properties. Among the three catalysts, Ti-Al-Mg exhibited the highest catalytic activity, with a maximum glycerol carbonate yield of 36.1%. This superior performance is attributed to the formation of a well-defined ternary oxide phase ($MgAl_2Ti_3O_{10}$), confirmed by XRD and XPS analyses. This phase reflects strong metal-oxygen interactions and a homogeneous distribution of Ti, Al, and Mg, as revealed by EDX mapping. The structural uniformity promotes a balanced distribution of active sites and reduces phase segregation, which are essential for efficient CO_2 activation and glycerol conversion.

In contrast, Ti-Fe-Mg and Ti-Cr-Mg formed binary spinel-type oxides ($MgFe_2O_4$, Cr_2MgO_4) and segregated metal oxide phases (Fe_2O_3, Cr_2O_3), without evidence of ternary phase formation. These structures led to surface heterogeneity and less uniform elemental dispersion, which limited the accessibility and effectiveness of active sites. The SEM images confirmed that both catalysts exhibited more agglomerated and fragmented morphologies, contributing to reduced surface exposure.

The acid-base character of the catalysts further explains the observed differences in performance. Ti-Al-Mg displayed a well acid-base balance due to the presence of weak Lewis acid sites from Al^{3+} and basic sites from Mg^{2+}. This balance favors the GC formation by facilitating CO_2 adsorption and minimizing side reactions. In contrast, Fe^{3+} and Cr^{3+} introduced stronger acidic sites, as supported by literature and indirectly confirmed by the catalytic behavior. The acidity in Ti-Fe-Mg and Ti-Cr-Mg promoted glycerol dehydration and polymerization side reactions, reducing the GC yield.

Textural analysis reinforced these trends. Ti-Al-Mg had the highest BET surface area (119.43 m^2/g) and a well-developed mesoporous structure, providing more accessible sites for reactants. Ti-Cr-Mg had a moderate surface area (54.47 m^2/g), while Ti-Fe-Mg exhibited the lowest (28.20 m^2/g), limiting its adsorption capacity despite a larger average pore size.

In summary, the findings confirm that optimal catalytic performance is achieved when the catalyst exhibits structural homogeneity, uniform dispersion of metal ions capable of forming stable ternary oxide phases, and a well-balanced acid-base surface. Ti-Al-Mg meets these conditions, resulting in superior activity. In contrast, the less organized structures and higher surface acidity of Ti-Cr-Mg and Ti-Fe-Mg limit their effectiveness. Consequently, the observed activity trend Ti-Al-Mg > Ti-Fe-Mg > Ti-Cr-Mg is directly correlated with these parameters.

5. Conclusions

This study demonstrates the successful synthesis, characterization and performance evaluation of three mixed metal oxide catalysts Ti-Al-Mg, Ti-Cr-Mg, and Ti-Fe-Mg, for the conversion of glycerol and CO_2 into glycerol carbonate via heterogeneous catalysis. Physicochemical analyses highlighted the superior textural properties of Ti-Al-Mg, including high surface area and uniform porosity. The crystalline surface composition was identified, and its acid-base characteristics were inferred from literature, all contributing to its enhanced catalytic activity.

Among the catalysts tested, Ti-Al-Mg exhibited the highest glycerol carbonate yield of 36.1% at 175 °C and 10 bar CO_2 over 4 hours, outperforming Ti-Fe-Mg and Ti-Cr-Mg. The high efficiency of Ti-Al-Mg is attributed to its optimal magnesium surface content, lower acidity, and improved CO_2 activation capacity. Conversely, Ti-Cr-Mg showed the lowest catalytic performance, mainly due to excessive acidity and limited active site accessibility.

Catalytic testing under varying temperatures and catalyst loadings further confirmed the superior performance of Ti-Al-Mg. Yield and conversion were enhanced up to a 10% catalyst concentration, although marginal improvements beyond 5% suggest a performance plateau likely limited by surface reaction kinetics limitations under tested reaction conditions.

Overall, Ti-Al-Mg is a promising catalyst for sustainable glycerol valorization through CO_2 utilization, providing an effective route toward green chemical synthesis.

References

1. Global Energy Review 2025. *Glob. Energy Rev. 2025* **2025**. https://doi.org/10.1787/a60abbf2-en.
2. Vasquez, W. V.; Hernández, D.M.; del Hierro, J.N.; Martin, D.; Cano, M.P.; Fornari, T. Supercritical Carbon Dioxide Extraction of Oil and Minor Lipid Compounds of Cake Byproduct from Brazil Nut (Bertholletia Excelsa) Beverage Production. *J. Supercrit. Fluids* **2021**, *171*, 105188. https://doi.org/10.1016/j.supflu.2021.105188.
3. IEA Putting CO 2 to Use. *Energy Rep.* **2019**, 86.
4. Lukato, S.; Kasozi, G.N.; Naziriwo, B.; Tebandeke, E. Glycerol Carbonylation with CO2 to Form Glycerol Carbonate: A Review of Recent Developments and Challenges. *Curr. Res. Green Sustain. Chem.* **2021**, *4*, 100199. https://doi.org/10.1016/j.crgsc.2021.100199.
5. Gao, Z.; Xiang, M.; He, M.; Zhou, W.; Chen, J.; Lu, J.; Wu, Z.; Su, Y. Transformation of CO2 with Glycerol to Glycerol Carbonate over ETS-10 Zeolite-Based Catalyst. *Molecules* **2023**, *28*, 1–13. https://doi.org/10.3390/molecules28052272.
6. Inrirai, P.; Keogh, J.; Centeno-Pedrazo, A.; Artioli, N.; Manyar, H. Recent Advances in Processes and Catalysts for Glycerol Carbonate Production via Direct and Indirect Use of CO2. *J. CO2 Util.* **2024**, *80*, 102693. https://doi.org/10.1016/j.jcou.2024.102693.
7. Ke, Y.H.; Xu, H.; Wang, X.; Liu, H.; Yuan, H. Production of Glycerol Carbonate by Coupling Glycerol and CO2 over Various Metal Oxide Catalyst. *J. CO2 Util.* **2024**, *83*. https://doi.org/10.1016/j.jcou.2024.102813.
8. Al-Kurdhani, J.M.H.; Wang, H. The Synthesis of Glycerol Carbonate from Glycerol and Carbon Dioxide over Supported CuO-Based Nanoparticle Catalyst. *Molecules* **2023**, *28*, 1–18. https://doi.org/10.3390/molecules28104164.
9. Ozorio, L.P.; Mota, C.J.A. Direct Carbonation of Glycerol with CO2 Catalyzed by Metal Oxides. *ChemPhysChem* **2017**, *18*, 3260–3265. https://doi.org/10.1002/cphc.201700579.
10. Li, H.; Gao, D.; Gao, P.; Wang, F.; Zhao, N.; Xiao, F.; Wei, W.; Sun, Y. The Synthesis of Glycerol Carbonate from Glycerol and CO2 over La2O2CO3-ZnO Catalysts. *Catal. Sci. Technol.* **2013**, *3*, 2801–2809. https://doi.org/10.1039/c3cy00335c.
11. Manuscript, A. *Nanoscale*; ISBN 9117225450.
12. Liu, J.; Li, Y.; Liu, H.; He, D. Transformation of CO2 and Glycerol to Glycerol Carbonate over CeO2–ZrO2 Solid Solution —— Effect of Zr Doping. *Biomass and Bioenergy* **2018**, *118*, 74–83. https://doi.org/10.1016/j.biombioe.2018.08.004.
13. Li, H.; Jiao, X.; Li, L.; Zhao, N.; Xiao, F.; Wei, W.; Sun, Y.; Zhang, B. Synthesis of Glycerol Carbonate by Direct Carbonylation of Glycerol with CO 2 over Solid Catalysts Derived from Zn/Al/La and Zn/Al/La/M (M = Li, Mg and Zr) Hydrotalcites. *Catal. Sci. Technol.* **2015**, *5*, 989–1005. https://doi.org/10.1039/C4CY01237B.
14. Xu, L.; Yang, Q.; Hu, L.; Wang, D.; Peng, Y.; Shao, Z.; Lu, C. Insights over Titanium Modified FeMgO x Catalysts for Selective Catalytic Reduction of NO x with NH 3 : **2019**, 14–18.
15. Teng, W.K.; Ngoh, G.C.; Yusoff, R.; Aroua, M.K. A Review on the Performance of Glycerol Carbonate Production via Catalytic Transesterification: Effects of Influencing Parameters. *Energy Convers. Manag.* **2014**, *88*, 484–497. https://doi.org/10.1016/j.enconman.2014.08.036.
16. Selvamani, T.; Anandan, S.; Asiri, A.M.; Maruthamuthu, P.; Ashokkumar, M. Preparation of MgTi2O5 Nanoparticles for Sonophotocatalytic Degradation of Triphenylmethane Dyes. *Ultrason. Sonochem.* **2021**,

75, 105585. https://doi.org/10.1016/j.ultsonch.2021.105585.

17. Ehsan, M.A.; Naeem, R.; McKee, V.; Hakeem, A.S.; Mazhar, M. MgTi2O5 Thin Films from Single Molecular Precursor for Photoelectrochemical Water Splitting. *Sol. Energy Mater. Sol. Cells* **2017**, *161*, 328–337. https://doi.org/10.1016/j.solmat.2016.12.015.
18. Scarpelli, F.; Mastropietro, T.F.; Poerio, T.; Godbert, N. Mesoporous TiO2 Thin Films: State of the Art. *Titan. Dioxide - Mater. a Sustain. Environ.* **2018**. https://doi.org/10.5772/intechopen.74244.
19. Umar, A.; Harraz, F.A.; Ibrahim, A.A.; Almas, T.; Kumar, R.; Al-Assiri, M.S.; Baskoutas, S. Iron-Doped Titanium Dioxide Nanoparticles as Potential Scaffold for Hydrazine Chemical Sensor Applications. *Coatings* **2020**, *10*, 1–13. https://doi.org/10.3390/coatings10020182.
20. Veiko, V.P.; Karlagina, Y.Y.; Samokhvalov, A.A.; Polyakov, D.S.; Manokhin, S.S.; Radaev, M.M.; Odintsova, G. V.; Gornushkin, I.B. Surface Structuring and Reverse Deposition of Nanoporous Titanium Oxides by Laser Ablation of Titanium in Air. *Plasma Chem. Plasma Process.* **2022**, *42*, 923–937. https://doi.org/10.1007/s11090-022-10256-0.
21. Cai, Y.; Shi, Q.; Wang, M.; Lv, X.; Cheng, Y.; Huang, W. Synthesis of Nanoscale Lambda-Ti3O5 via a PEG Assisted Sol-Gel Method. *J. Alloys Compd.* **2020**, *848*, 156585. https://doi.org/10.1016/j.jallcom.2020.156585.
22. Rani, N.; Chahal, S.; Chauhan, A.S.; Kumar, P.; Shukla, R.; Singh, S.K. X-Ray Analysis of MgO Nanoparticles by Modified Scherer's Williamson-Hall and Size-Strain Method. *Mater. Today Proc.* **2019**, *12*, 543–548. https://doi.org/10.1016/j.matpr.2019.03.096.
23. Al-hadeethi, Y.; Sayyed, M.I. E Ff Ect of Gd 2 O 3 on the Radiation Shielding Characteristics Of. *Ceram. Int.* **2020**, *185*, 0–1.
24. Karan, P.; Chakraborty, R. E-Waste Derived Silica-Alumina for Eco-Friendly and Inexpensive Mg-Al-Ti Photocatalyst towards Glycerol Carbonate (Electrolyte) Synthesis: Process Optimization and LCA. *Waste Manag.* **2022**, *140*, 213–224. https://doi.org/10.1016/j.wasman.2021.11.022.
25. Xing, Y.; Shen, X.; Niu, Q.; Duan, H.; Tang, C.; Tao, B.; Chen, S.; Shangguan, Q.; Feng, B.; Yu, H.; et al. Thermally and Chemically Stable Fe/Mg-Layered Double Oxides-Biochar for Enhanced Polystyrene Nanoplastic Adsorption and Sustainable Recycling. *Chem. Eng. J.* **2025**, *508*, 160918. https://doi.org/10.1016/j.cej.2025.160918.
26. Liu, J.; Zang, P.; Liu, X.; Mi, J.; Wang, Y.; Zhang, G.; Chen, J.; Zhang, Y.; Li, J. A Novel Highly Active Catalyst Form CuFeMg Layered Double Oxides for the Selective Catalytic Reduction of NO by CO. *Fuel* **2022**, *317*, 123469. https://doi.org/10.1016/j.fuel.2022.123469.
27. Zainuri, M. Hematite from Natural Iron Stones as Microwave Absorbing Material on X-Band Frequency Ranges. *IOP Conf. Ser. Mater. Sci. Eng.* **2017**, *196*. https://doi.org/10.1088/1757-899X/196/1/012008.
28. Gibot, P. Centimetric-Sized Chromium (III) Oxide Object Synthesized by Means of the Carbon Template Replication. *Ceramics* **2020**, *3*, 92–100. https://doi.org/10.3390/ceramics3010010.
29. Mallesham, B.; Rangaswamy, A.; Rao, B.G.; Rao, T.V.; Reddy, B.M. Solvent-Free Production of Glycerol Carbonate from Bioglycerol with Urea Over Nanostructured Promoted SnO2 Catalysts. *Catal. Letters* **2020**, *150*, 3626–3641. https://doi.org/10.1007/s10562-020-03241-9.
30. Kloprogge, J.T. X-Ray Photoelectron Spectroscopy (XPS) Study of Layered Double Hydroxides with Different Exchangeable Anions. *Appl. Sci.* **2025**, *15*. https://doi.org/10.3390/app15031318.
31. Chen, J.; Song, Y.; Shan, D.; Han, E.H. In Situ Growth of Mg-Al Hydrotalcite Conversion Film on AZ31 Magnesium Alloy. *Corros. Sci.* **2011**, *53*, 3281–3288. https://doi.org/10.1016/j.corsci.2011.06.003.
32. Suzuki, Y.; Shinoda, Y. Magnesium Dititanate (MgTi2O5) with Pseudobrookite Structure: A Review. *Sci. Technol. Adv. Mater.* **2011**, *12*. https://doi.org/10.1088/1468-6996/12/3/034301.
33. Jayanthi, S.; Kutty, T.R.N. Microwave Dielectric Properties of Mg4Al2Ti9O25 Ceramics. *Mater. Lett.* **2008**,

62, 556–560. https://doi.org/10.1016/j.matlet.2007.06.013.

34. Akaogi, M.; Ishii, T.; Yamaura, K. Post-Spinel-Type AB2O4 High-Pressure Phases in Geochemistry and Materials Science. *Commun. Chem.* **2024**, *7*. https://doi.org/10.1038/s42004-024-01278-0.
35. Pilania, G.; Kocevski, V.; Valdez, J.A.; Kreller, C.R.; Uberuaga, B.P. Prediction of Structure and Cation Ordering in an Ordered Normal-Inverse Double Spinel. *Commun. Mater.* **2020**, *1*, 1–11. https://doi.org/10.1038/s43246-020-00082-2.
36. Liu, R.; Conradie, J.; Erasmus, E. Comparison of X-Ray Photoelectron Spectroscopy Multiplet Splitting of Cr 2p Peaks from Chromium Tris(β-Diketonates) with Chemical Effects. *J. Electron Spectros. Relat. Phenomena* **2016**, *206*, 46–51. https://doi.org/10.1016/j.elspec.2015.11.006.
37. Lee, H.; Aytuna, Z.T.; Bhardwaj, A.; Wilhelm, M.; Khan, L.; May, B.; Mueller, D.N.; Mathur, S. Controlling Degree of Inversion in MgFe2O4 Spinel Films Grown in External Magnetic Fields. *Adv. Eng. Mater.* **2023**, *25*, 2–9. https://doi.org/10.1002/adem.202300021.
38. Ishii, T.; Miyajima, N.; Sinmyo, R.; Kojitani, H.; Mori, D.; Inaguma, Y.; Akaogi, M. Discovery of New-Structured Post-Spinel MgFe2O4: Crystal Structure and High-Pressure Phase Relations. *Geophys. Res. Lett.* **2020**, *47*, 1–9. https://doi.org/10.1029/2020GL087490.
39. Wu, L.; Li, Y.; Fu, Z.; Su, B.L. Hierarchically Structured Porous Materials: Synthesis Strategies and Applications in Energy Storage. *Natl. Sci. Rev.* **2020**, *7*, 1667–1701. https://doi.org/10.1093/nsr/nwaa183.
40. Perego, C.; Millinib, R. Porous Materials in Catalysis: Challenges for Mesoporous Materials. *Chem. Soc. Rev.* **2013**, *42*, 3956–3976. https://doi.org/10.1039/c2cs35244c.
41. Granados-Reyes, J.; Salagre, P.; Cesteros, Y. CaAl-Layered Double Hydroxides as Active Catalysts for the Transesterification of Glycerol to Glycerol Carbonate. *Appl. Clay Sci.* **2016**, *132–133*, 216–222. https://doi.org/10.1016/j.clay.2016.06.008.
42. Wang, D.; Zhu, Q.; Xing, Z.; Fang, L. Control of Chloride Ion Corrosion by MgAlOx/MgAlFeOx in the Process of Chloride Deicing. *Environ. Sci. Pollut. Res.* **2022**, *29*, 9269–9281. https://doi.org/10.1007/s11356-021-16205-2.
43. Thommes, M.; Kaneko, K.; Neimark, A. V.; Olivier, J.P.; Rodriguez-Reinoso, F.; Rouquerol, J.; Sing, K.S.W. Physisorption of Gases, with Special Reference to the Evaluation of Surface Area and Pore Size Distribution (IUPAC Technical Report). *Pure Appl. Chem.* **2015**, *87*, 1051–1069. https://doi.org/10.1515/pac-2014-1117.
44. CHEN, K.; ZHANG, T.; CHEN, X.; HE, Y.; LIANG, X. Model Construction of Micro-Pores in Shale: A Case Study of Silurian Longmaxi Formation Shale in Dianqianbei Area, SW China. *Pet. Explor. Dev.* **2018**, *45*, 412–421. https://doi.org/10.1016/S1876-3804(18)30046-6.
45. Yadav, G.D.; Chandan, P.A. A Green Process for Glycerol Valorization to Glycerol Carbonateover Heterogeneous Hydrotalcite Catalyst. *Catal. Today* **2014**, *237*, 47–53. https://doi.org/10.1016/j.cattod.2014.01.043.
46. Manuscript, A. Catalysis Science & Echnology. **2020**. https://doi.org/10.1039/D0CY01821J.
47. Tsuzuki, R.; Ichikawa, K.; Kase, M. *[CONTRIBUTION FROM THE RESEARCH AND DEVELOPMENT DIVISIOK OF DAINIPPON PRINTING INK MFG New Reactions of Organic Isocyanates. I. Reaction with Alkylene Carbonates*;
48. Galadima, A.; Muraza, O. Sustainable Production of Glycerol Carbonate from By-Product in Biodiesel Plant. *Waste and Biomass Valorization* 2017, *8*, 141–152.
49. Rousseau, J.; Rousseau, C.; Lynikaite, B.; Šačkus, A.; de Leon, C.; Rollin, P.; Tatibouët, A. Tosylated Glycerol Carbonate, a Versatile Bis-Electrophile to Access New Functionalized Glycidol Derivatives. *Tetrahedron* **2009**, *65*, 8571–8581. https://doi.org/10.1016/j.tet.2009.07.095.

50. Mosallanejad, S.; Dlugogorski, B.Z.; Kennedy, E.M.; Stockenhuber, M. On the Chemistry of Iron Oxide Supported on γ-Alumina and Silica Catalysts. *ACS Omega* **2018**, *3*, 5362–5374. https://doi.org/10.1021/acsomega.8b00201.
51. Benoit, M.; Brissonnet, Y.; Guélou, E.; De-Oliveira-Vigier, K.; Barrault, J.; Jérôme, F. Acid-Catalyzed Dehydration of Fructose and Inulin with Glycerol or Glycerol Carbonate as Renewably Sourced Co-Solvent. *ChemSusChem* **2010**, *3*, 1304–1309. https://doi.org/10.1002/cssc.201000162.
52. Ursin, C.; Hansen, C.M.; Van Dyk, J.W.; Jensen, P.O.; Christensen, I.J.; Ebbehoej, J. Permeability of Commercial Solvents Through Living Human Skin. *Am. Ind. Hyg. Assoc. J.* **1995**, *56*, 651–660. https://doi.org/10.1080/15428119591016665.
53. Tudorache, M.; Protesescu, L.; Coman, S.; Parvulescu, V.I. Efficient Bio-Conversion of Glycerol to Glycerol Carbonate Catalyzed by Lipase Extracted from Aspergillus Niger. *Green Chem.* **2012**, *14*, 478–482. https://doi.org/10.1039/c2gc16294f.

Disclaimer/Publisher's Note: The statements, opinions and data contained in all publications are solely those of the individual author(s) and contributor(s) and not of MDPI and/or the editor(s). MDPI and/or the editor(s) disclaim responsibility for any injury to people or property resulting from any ideas, methods, instructions or products referred to in the content.